Emission spectra of Rb*He$_n$ exciplexes in a cold ^{4}He gas

K. Hirano, K. Enomoto, M. Kumakura, Y. Takahashi, and T. Yabuzaki*

Department of Physics, Graduate School of Science, Kyoto University, Kyoto 606-8502, Japan

We report on the systematic observation of emission spectra of Rb*He$_n$ exciplexes ($n=1,2,\ldots,6$), realized by exciting Rb atoms to the $5\,^2P$ states (Rb*) in a cold ^{4}He gas. The observed broad spectral components are assigned to Rb*He$_n$ ($n=1-6$) using theoretical spectra obtained from *ab initio* potential curves. The dynamics of the exciplex formation is discussed, based on the observed temperature dependence of the spectra. The He gas density dependence of the spectra of Rb*He is understood as a change in the population distribution over the vibrational levels. The present results are compared with our previous work with Cs [K. Enomoto *et al.*, Phys. Rev. A **66**, 042505 (2002)], and differences are explained in terms of the difference in the fine-structure splitting. Furthermore, we show the emission spectrum observed after the excitation of Rb in liquid He and conclude that it is the fluorescence from the exciplex Rb*He$_6$.

I. INTRODUCTION

Alkali-metal atoms excited to the first P states in a cold He environment produce alkali-metal–He$_n$ exciplexes. The exciplex formation was discussed in order to give an explanation on the fact that the D emission lines were not observed from excited light alkali-metal atoms (Li, Na, K) in liquid He [1,2]. Kanorsky *et al.* and Dupont-Roc have proposed a model that several He atoms are localized at the place where the valence electron density of the alkali-metal atom is small [3,4]. Dupont-Roc paid attention to the spin-orbit coupling in the P state of alkali-metal atoms, and dealt with two typical cases, Cs and Na [4]. He discussed separately two fine structure components of Cs ($6\,^2P_{3/2}$ and $6\,^2P_{1/2}$), based on the fact that the fine-structure splitting Δ of the $6\,^2P$ states (554.0 cm^{-1}) is large compared to the splitting induced by an interaction with liquid He. He pointed out that the valence electron of Cs($6\,^2P_{3/2}$) holds the applelike density distribution and only two He atoms can stick to the Cs core along the nodal line. On the other hand, due to the small fine-structure splitting, the orbital of the valence electron of Na is well expressed by a p_z orbital, and five or six He atoms are localized on a ring on the nodal plane of the valence electron orbital.

In our previous studies of Rb in the $5\,^2P$ states (hereafter simply written as Rb*) in superfluid ^{4}He, pressure-dependent quenching of the D_1 emission line ($5\,^2P_{1/2} \rightarrow 5\,^2S_{1/2}$) was observed [5]. This phenomenon is considered to be due to the pressure dependent decay process from the $5\,^2P_{1/2}$ state to the exciplex Rb*He$_n$ which may emit infrared fluorescence. The Rb*He$_n$ exciplex was predicted to have the Na*He$_n$-type configuration, that is, n He atoms form a ring around Rb*, since no emission line was observed at the spectral region where the emission from Rb*He$_2$ is expected to be seen. The number n of He atoms was roughly estimated to be about six under the assumption that the distance between neighboring He atoms is equal to

that in liquid He [5]. We searched for the emission spectrum of Rb*He$_n$ in liquid He over an infrared region and found a broad emission band with a peak at 7000 cm^{-1}. This experimental result will be briefly presented in this paper. This band was the only spectrum of exciplex we could observe, and emission from smaller exciplexes was absent. The absence of the emission from smaller exciplexes indicates that the formation rates of exciplexes in liquid He are much faster than their radiative decay rates due to the high atom density of liquid He, and only the terminal exciplex is observed in liquid He. In the following, we will write the number of He atoms in the exciplex observed in liquid He as n_{max}. If the emission spectra of the intermediate exciplexes Rb*He$_n$ ($1 \le n < n_{max}$) can be observed, the value of n_{max} may be determined accurately. Recently, Brühl *et al.* have observed the emission spectrum of Rb*He detached from He droplets [6]. The spectra for $2 \le n < n_{max}$, however, have not been observed so far.

The main purpose of this paper is to present the emission spectra of Rb*He$_n$ ($n=1,2,\ldots,n_{max}$) observed in a cold glass cell containing Rb atoms and a He gas. The He density in the cell is, in the present case, two orders of magnitude less than in liquid He, so that the formation rates of the exciplexes become comparable to their radiative decay rates, which enables us to observe the emission spectra of the intermediate exciplexes. Such an observation of the spectrum of intermediate exciplex was first made for Ag by Jakubek *et al.* [7]: they observed emission spectra of Ag*He$_n$ ($n=1,2$) in a cold He gas, although the emission from $n=1$ was absent in liquid He [8]. We recently reported emission spectra of Cs*He$_n$ ($n=1,2$) [9]. The spectrum of Cs*He, which was also absent in liquid He, could be observed by the use of the He gas environment.

Another interest of the present work concerns the dynamics of the exciplex formation (Rb*$\rightarrow$Rb*He$\rightarrow\cdots$ $\rightarrow$Rb*He$_{n_{max}}$). We investigate the dynamics by observing the temperature dependence of the emission spectra. It should be mentioned that, in the present experiment, the temperature and the He density can be changed over a wide range, which is in contrast to experiments with liquid He or

*Electronic address: yabuzaki@scphys.kyoto-u.ac.jp

He droplets. This helps us to study not only the dynamics of the exciplex formation but also the dynamics of relaxation processes induced by collisions with He atoms. In the present work, we evaluate the rate coefficient for the fine-structure relaxation of Rb*He.

We are also interested in comparing the results of the present work and our previous experiment with Cs [9]. A remarkable difference is that Rb has larger n_{max} than Cs ($n_{max}=2$). The spin-orbit coupling strength should concern this difference and a quantitative study on the influence of the spin-orbit interaction is needed to explain the difference in n_{max} between Rb and Cs, since the splitting Δ of Cs is on the same order of magnitude as that of the Rb-5 ^2P states (237.6 cm^{-1}) and the difference in potential energy between the pairs Cs*-He and Rb*-He is not so large (see, for example, potentials in Ref. [10]). Thus, in the present work, we calculate potential-energy surfaces for the systems Rb*He$_2$-He and Cs*He$_2$-He taking into account the spin-orbit interaction, and consider the difference in the formation of $n=3$.

The paper is organized as follows. In Sec. II, we show theoretical emission spectra of Rb*He$_n$ calculated from *ab initio* potential curves. In Sec. III, we describe the experimental method. In Sec. IV, we first present the experimental results (Sec. IV A), and assign the observed spectra (Sec. IV B). Next, we describe the temperature dependence of the spectra (Sec. IV C), with which we discuss the dynamics of the exciplex formation (Sec. IV D). We also show analysis on the He gas density dependence of the spectra of Rb*He (Sec. IV E). Finally, we discuss differences between the results for Rb and Cs (Sec. IV F).

II. THEORETICAL EMISSION SPECTRA

We calculated theoretical emission spectra of Rb*He$_n$ ($n=1-7$). With respect to the potential energies of Rb*He$_n$, we carried out *ab initio* calculations with the MOLPRO program package [11], using the 3-21G* basis set [12] for the Rb atom and the 6-31G** basis set [13] for the He atoms.

To obtain emission spectra of Rb*He, we first calculated potential curves of the lowest two $^2\Sigma$ and one $^2\Pi$ states of Rb*He. At each value of internuclear distance r, energies of the three states were calculated by a sequence of the restricted Hartree-Fock (RHF) calculation, the multiconfiguration self-consistent field calculation [14], and the internally contracted multireference configuration interaction calculation [15]. With respect to the potential energies of the excited states, we took into account the spin-orbit interaction of the Rb-5 ^2P states ($\Delta=237.6$ cm^{-1}), based on the assumption that it is independent of the internuclear distance r [16]. We consider that this assumption is quite valid for Rb*He$_n$. To the best of our knowledge, there is no study on the fine-structure of a Rb–rare-gas exciplex or complex. There are, however, several studies on the complex of Na and a heavy rare-gas atom (Ar, Kr, Xe) [17–20]. According to these studies, with decreasing the mass of rare-gas atoms, i.e., decreasing the polarizability, the fine-structure splitting of the Na–rare-gas complexes comes close to the value expected from
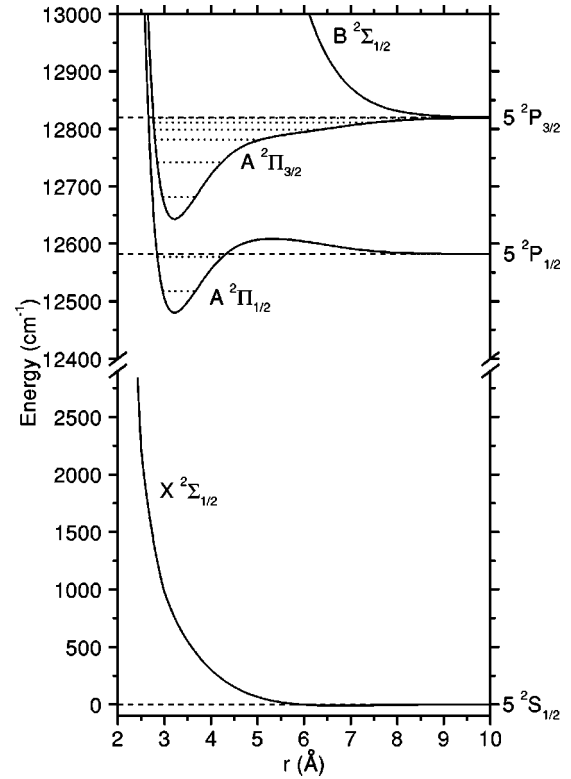
FIG. 1. Theoretical Rb-He potential curves of the ground state ($X\,^2\Sigma_{1/2}$) and the excited states ($A\,^2\Pi_{1/2}$, $A\,^2\Pi_{3/2}$, and $B\,^2\Sigma_{1/2}$) obtained from *ab initio* calculations. Dotted lines show the vibrational energy levels (see also Table I). Asymptotic energies of the potentials are shown by dashed lines, which are labeled on the right-hand side by atomic states of Rb.

this assumption, which is $\frac{2}{3}\Delta$ in Hund's case (a). The deviation from the assumption is less than $\sim 30\%$ even for Ar [17,18], so it is natural to consider that the deviation for He should be much smaller than that for Ar because of the small polarizability of He which is about eight times smaller than that of Ar [21]. The potential curves of the excited states were shifted so that they coincided with the energy levels of Rb + He in the $r\rightarrow\infty$ limit. Figure 1 shows the potential curves obtained for the ground state $X\,^2\Sigma_{1/2}$ and the excited states $A\,^2\Pi_{1/2}$, $A\,^2\Pi_{3/2}$, and $B\,^2\Sigma_{1/2}$. The repulsive $B\,^2\Sigma_{1/2}$ and attractive $A\,^2\Pi_{3/2}$ states correlate to the asymptotic state Rb($5\,^2P_{3/2}$) + He. The $A\,^2\Pi_{3/2}$ potential has the minimum at $r=3.21$ Å with a depth of 176.8 cm^{-1} below the dissociation limit. The potential of the $A\,^2\Pi_{1/2}$ state correlating to Rb($5\,^2P_{1/2}$) + He also has the minimum at $r=3.21$ Å with a depth of 102.1 cm^{-1} below the dissociation limit. The $A\,^2\Pi_{1/2}$ potential exhibits a potential barrier at $r=5.3$ Å with a height of 26.5 cm^{-1} above the dissociation limit. This barrier would prevent the entrance of the He atom into the potential well, when the Rb atom is excited to the $5\,^2P_{1/2}$ state at about liquid He temperatures.

With the help of the BCONT 2.0 program code [22], we numerically calculated the vibrational wave function $\psi'(r)$ for the excited states $A\,^2\Pi_{1/2}$ and $A\,^2\Pi_{3/2}$, and then calculated emission spectra $I(\nu)$ for the transitions from the obtained vibrational levels to the ground state $X\,^2\Sigma_{1/2}$ using the

TABLE I. Vibrational levels in the $A\ ^2\Pi_{3/2}$ and $A\ ^2\Pi_{1/2}$ states of Rb*He. The energies are given relative to the dissociation limits Rb($5\ ^2P_{3/2}$)+He and Rb($5\ ^2P_{1/2}$)+He, respectively.

	Vibrational level	Energy (cm^{-1})
$A\ ^2\Pi_{3/2}$	$v=5$	-1.1
	$v=4$	-9.0
	$v=3$	-20.9
	$v=2$	-39.1
	$v=1$	-78.3
	$v=0$	-138.8
$A\ ^2\Pi_{1/2}$	$v=1$	-5.2
	$v=0$	-64.4

relation $I(\nu)\propto\nu^3|\int\psi'(r)\psi(r;\nu)dr|^2$, where $\psi(r;\nu)$ is the continuum wave function for the repulsive $X\ ^2\Sigma_{1/2}$ state and ν is the transition frequency. Table I shows the calculated energies of the vibrational levels. The states $A\ ^2\Pi_{3/2}$ and $A\ ^2\Pi_{1/2}$ have six and two levels, respectively. Figure 2 shows the calculated emission spectrum for each vibrational level. Here we have assumed that the transition dipole moment of Rb*He is equal to that of Rb. With the *ab initio* calculation, we confirmed that the transition moment changes only 3% in the range $r>2.5$ Å.

We obtained emission spectra also from Pascale's Rb-He potential curves [10], taking into account the spin-orbit in-
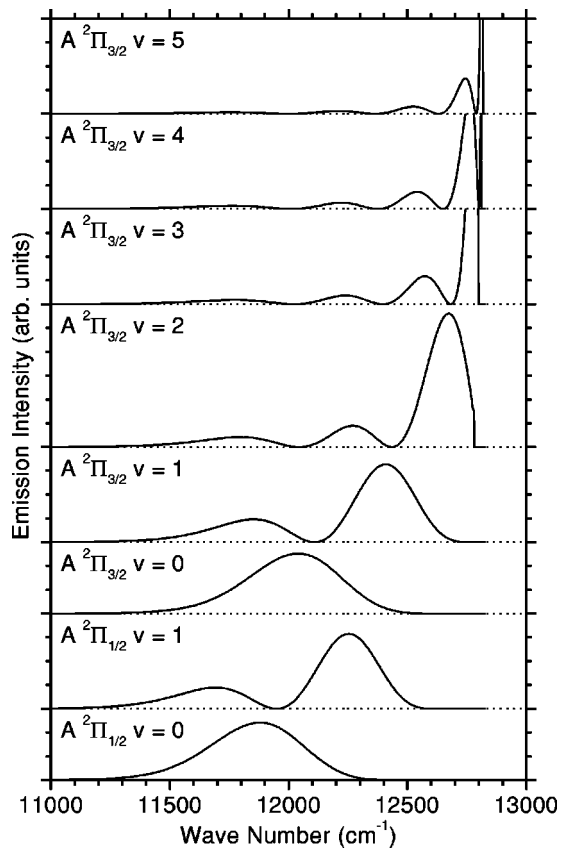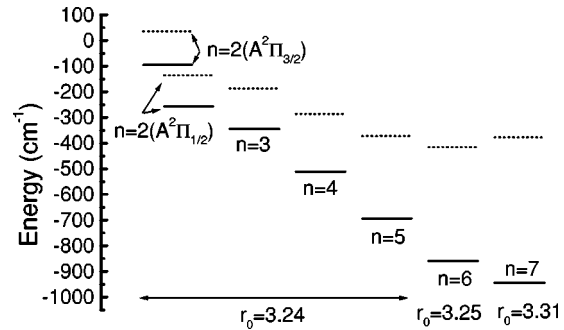
FIG. 3. Potential energy E'_n at the bottom of the potential well (solid lines) and the energy level E_n of the vibrational ground state (dotted lines) in the first electronic excited state for each n. The equilibrium radius r_0 in units of Å is also shown.

teraction. However, the results were found to be in worse agreement with experimental spectra than the spectra obtained from the *ab initio* potentials: the peak position of the emission spectrum from the $A\ ^2\Pi_{1/2}$ $v=0$ state was calculated to be 11 880 cm^{-1} and 12 018 cm^{-1} from the *ab initio* and Pascale's potentials, respectively, whereas the peak was observed at 11 820 cm^{-1} as shown later.

We calculated emission spectra of Rb*He$_n$ ($n=2-7$) under the assumption that n He atoms are located equidistantly on a circle with the center at the position of Rb. We calculated at the RHF level *ab initio* Rb-He$_n$ potential curves as functions of the radius r of the circle [11], and took into account the spin-orbit interaction [16]. The equilibrium radius r_0 obtained for each potential curve is shown in Fig. 3. It should be noted that, for $n=2$, the lowest two of the three excited states ($A\ ^2\Pi_{1/2}$ and $A\ ^2\Pi_{3/2}$) have attractive potentials, whereas for $n\geq3$, only the lowest state has attractive potential.

For $n\geq3$, the energy difference between the lowest two excited states before the consideration of the spin-orbit interaction is larger than 10Δ at $r=r_0$. As a result, with respect to the lowest excited state, more than 99% of the Rb valence electron occupies the p_z orbital which has the z axis along the axis of the circle, even after the spin-orbit interaction is considered. So it can be said that the spin-orbit coupling is substantially decoupled for $n\geq3$.

For each potential curve obtained for the attractive electronic state of Rb*He$_n$, we calculated the energy of the vibrational ground state, and obtained emission spectrum from the state. The calculation procedure is as follows. First we calculated the vibrational wave function $\psi'_{sym}(r)$ for the symmetric vibration mode, which originates from the variation of r, and a function $I'(\nu)$ $\propto\nu^3|\int\psi'_{sym}(r)\psi_{sym}(r;\nu)dr|^2$ with the help of the BCONT 2.0 program [22], where $\psi_{sym}(r;\nu)$ is the continuum wave function for the symmetric motion in the electronic ground state. In addition, taking into account all vibrational modes, we calculated at the RHF level the sum ϵ of the zero-point energies for all the other vibrational modes [11,23]. The spin-orbit coupling was neglected in the calculation of ϵ for n $=3-7$, because it is substantially decoupled as mentioned above. Then we approximated the emission spectrum as

FIG. 2. Theoretical emission spectra from the vibrational levels of Rb*He.
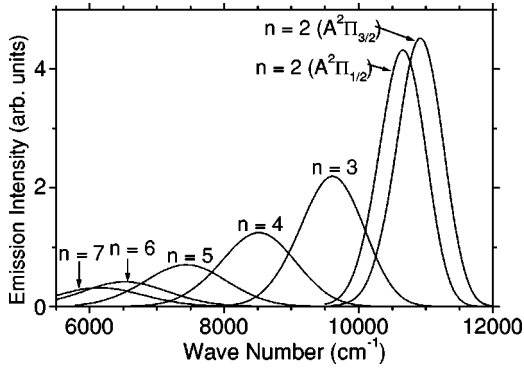
FIG. 4. Theoretical emission spectrum of Rb*He$_n$ ($n=2$–7) calculated for the transition from the vibrational ground state. For $n=2$, initial electronic state is indicated in parentheses.

$I'(\nu-\epsilon)$, that is, the function $I'(\nu)$ was shifted toward larger wave number by the amount of ϵ. The calculated emission spectra are shown in Fig. 4, where we see that the emission spectrum exhibits a redshift, broadening, and a decrease in the integrated intensity, as n increases. The redshift is mainly due to the increase in the repulsive energy of the ground state. The broadening is attributed to the increase in the slope of the repulsive wall of the ground-state potential. The emission intensity becomes weak as the transition energy ν is decreased, because the radiative transition rate is proportional to ν^3.

We show in Fig. 3 the potential energy E'_n at the bottom of the potential well and the energy E_n of the vibrational ground state, for each exciplex. The value $E_n-E'_n$ corresponds to the total zero-point energy. Let us consider here the maximum number of sticking He atoms, n_{max}. We consider that the number n_{max} is the maximum value of n satisfying the relation $\Delta E_n=E_{n-1}-E_n>0$. The energy differences are obtained as $\Delta E_4=99.5$ cm^{-1}, $\Delta E_5=85.8$ cm^{-1}, $\Delta E_6=43.9$ cm^{-1}, and $\Delta E_7=-38.7$ cm^{-1}. Therefore, it is suggested from this theoretical consideration that the number n_{max} is 6.

III. EXPERIMENTAL SETUP AND PROCEDURE

The experimental setup is illustrated in Fig. 5(a). A Pyrex glass cell (cubic: $2\times2\times2$ cm^3) containing a small amount of Rb metal was mounted in a pumped liquid He cryostat with optical glass windows. The cell was filled with 730 torr ^{4}He gas at the liquid N$_2$ temperature (77 K) and was sealed. The cell temperature T was varied from about 1.3 K to room temperature, and it was monitored with a calibrated sensor placed near the cell. The He gas density in the cell is constant (9×10^{19} cm^{-3}) above the condensation temperature $T_c=1.9$ K, whereas it decreases as T falls below T_c, following the saturated vapor pressure of He [see Fig. 5(b)]. Gaseous Rb atoms in the cryogenic cell were produced with the laser ablation method, in which the second harmonic of a Q-switched Nd:YLiF$_4$ (YLF) laser (wavelength 523 nm, repetition rate 1 kHz, and pulse energy 100 μJ) was focused on a small area of the cell wall covered with a thin film or small particles of Rb. Within a few seconds, we obtained a Rb
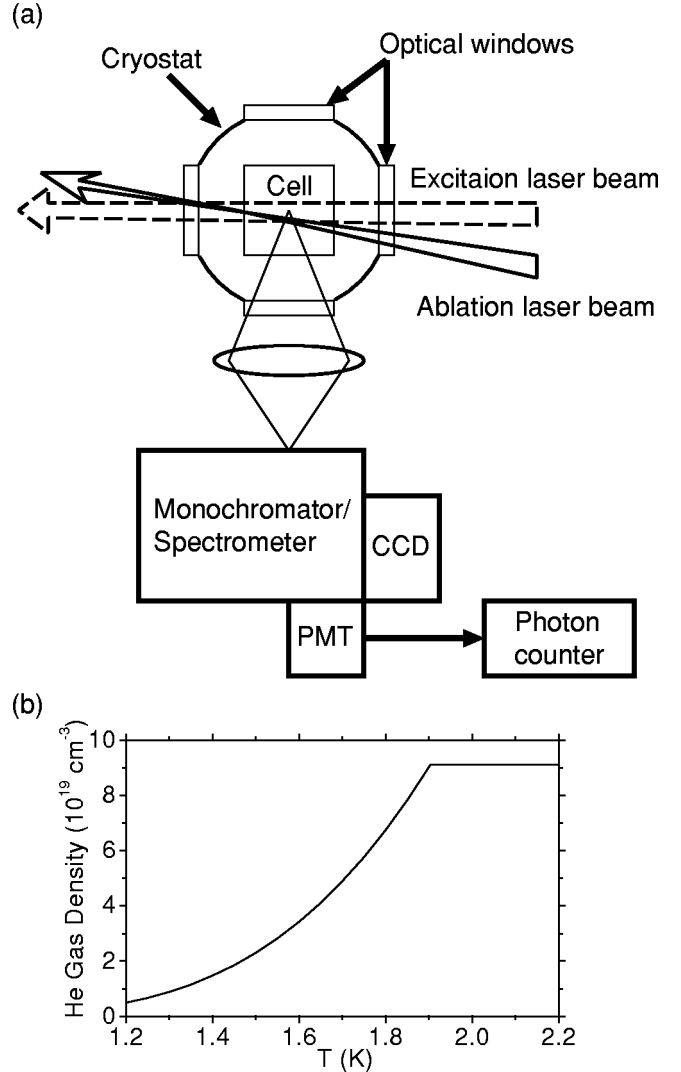
FIG. 5. (a) Experimental setup. (b) He gas density in the cell as a function of T.

vapor at a density of 10^8–10^{10} cm^{-3}. Details of our cryostat system and the procedure of preparing the cell have been reported already [24]. In the present work, we did not use the light-induced atom desorption method reported in Ref. [24], since it is not effective in producing alkali-metal vapors at $T>T_c$.

The Rb atoms produced in this way were excited with a diode laser through either the D_2 transition ($5\,^2S_{1/2}\rightarrow5\,^2P_{3/2}$, 12 820 cm^{-1}) or the D_1 transition ($5\,^2S_{1/2}\rightarrow5\,^2P_{1/2}$, 12 582 cm^{-1}). The typical intensity of the diode laser beam was 0.2 W/cm^2 in front of the cell. The fluorescence introduced to a monochromator was detected with an infrared-sensitive photomultiplier tube (PMT) (Hamamatsu, R5509-71) and a photon counter. The PMT has sufficient sensitivity in the wave number range down to about 6000 cm^{-1}. The spectral resolution of our monochromator-PMT system was ≈150 cm^{-1}. To obtain higher resolution for the spectral range down to about 10 000 cm^{-1}, we introduced the fluorescence to a spectrometer and detected with a charge-coupled-device (CCD) (Princeton instruments, LN/
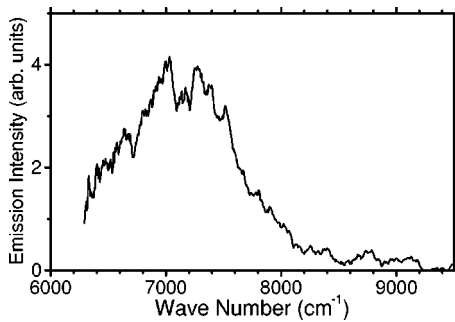
FIG. 6. Emission spectrum of Rb*He$_{n_{max}}$ in liquid He.

FIG. 7. Emission spectra observed in the cases of the D_2 excitation (a) and D_1 excitation (b) at different temperatures. Vertical dotted lines labeled as a–f indicate experimentally obtained peak positions of spectral components for Rb*He$_n$ ($n = 1$–6). They are located at 11 820 cm^{-1}, 10 810 cm^{-1}, 9949 cm^{-1}, 9105 cm^{-1}, 8065 cm^{-1}, and 7300 cm^{-1}, respectively (see Sec. IV B).

CCD-1100PF). This spectrometer-CCD system measures a wide-ranging spectrum ($\gtrsim 2000$ cm^{-1}) at once, without the influence of fluctuation of the Rb vapor density. Therefore, we could obtain a better signal to noise ratio with higher resolution of about 20 cm^{-1}, than in the case of the monochromator-PMT system. The detection systems have been calibrated with a commercial standard lamp. All the measured spectra have been normalized by the emission intensity integrated over the measured spectral range.

In this paper, we also present an emission spectrum of Rb*He$_n$ in liquid He observed in an infrared region. The experimental setup for the observation of this spectrum was almost the same as that of Ref. [25]. Rb metal immersed in superfluid liquid He at the temperature of 1.88 K was ablated with the YLF pulse laser. Rb atoms isolated in liquid He were excited by a cw Ti:Al$_2$O$_3$ laser beam tuned to the D_2 line (wave number 13 072 cm^{-1}). With a dark period of 50 μs for thermalization after each ablation pulse, the fluorescence from Rb*He$_n$ was detected with the PMT and the photon counting system.

IV. RESULTS AND DISCUSSION

A. Overview of experimental results

At first, we show the emission spectrum of Rb*He$_n$ in liquid He in Fig. 6. In addition to this infrared emission, the D_1 emission line of Rb* is observed at about 12 600 cm^{-1} in liquid He [25]. This broadband infrared spectral component peaks at about 7100 cm^{-1} and has a full width at half maximum (FWHM) of about 1230 cm^{-1}. This is the emission spectrum from the terminal exciplex Rb*He$_{n_{max}}$. It is important to note that there is no other spectral component between this broadband component and the D_1 emission line.

The emission spectra of Rb*He$_n$ observed in cryogenic gaseous He are shown in Figs. 7(a) and 7(b) in the cases of the D_2 and D_1 excitation, respectively. They were observed with the monochromator-PMT system. The observed spectra consist of several broad spectral components in addition to the sharp D lines of Rb. These components are assigned to the emission from Rb*He$_n$, as described in detail in Sec. IV B. With respect to the peak positions or widths of the components, difference cannot be seen between the spectra for the D_2 and D_1 excitations. Particularly for the two components at about 11 800 cm^{-1} and 10 800 cm^{-1}, we con-

firmed this by measuring better resolved spectra with the spectrometer-CCD system. We found in this measurement that the former had a peak at 11 820 cm^{-1} and the FWHM of 610 cm^{-1} and the latter 10 810 cm^{-1} and 670 cm^{-1}, respectively.

He gas density in the cell is constant (9×10^{19} cm^{-3}) in the temperature range $T \gtrsim 2$ K shown in Figs. 7(a) and 7(b). Nevertheless, the emission spectra observed are strongly dependent on T. In Fig. 7(b) showing the result of the D_1 excitation, no spectral components except the D_1 emission line can be observed at $T \lesssim 5$ K, but broad components of Rb*He$_n$ appear as T rises above 5 K. This is different from the D_2 excitation case, in which broad components can be seen even at $T \lesssim 5$ K. Apart from this difference, the broad emission spectra in both cases of the D_2 and D_1 excitations are dependent on T in the same manner.

(1) The ratio of the integrated intensity of the emission from Rb*He$_n$ to the total emission intensity has a maximum of about 50% at $T \approx 25$ K. The ratio decreases with increasing T above 25 K, and at 100 K it is about 6%.

(2) At $T \lesssim 10$ K, the spectra consist mainly of the components at 11 820 cm^{-1}, 10 810 cm^{-1}, and 7300 cm^{-1}. As T increases above 10 K, the broad spectrum at 7300 cm^{-1} seems to shift toward larger wave number, until it merges into the component at 11 820 cm^{-1} at $T \approx 40$ K.
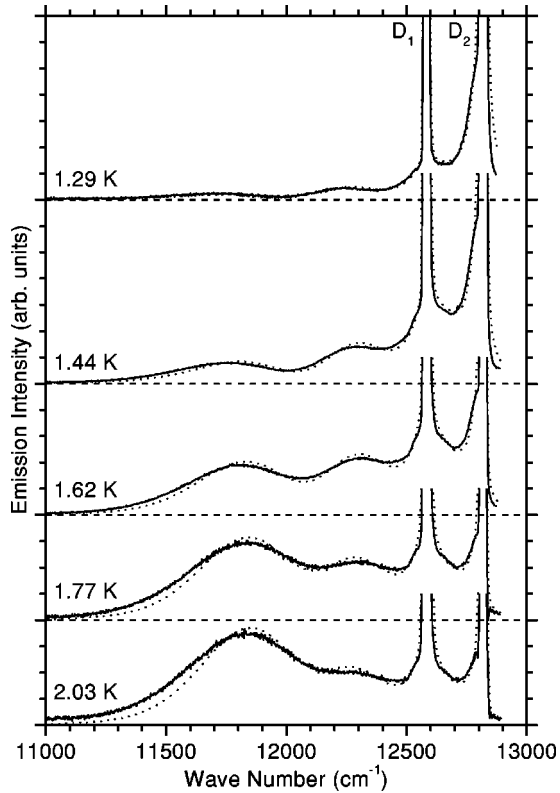
FIG. 8. Emission spectra observed in the case of the D_2 excitation (solid lines). The dotted lines show the best-fitted curves, which are composed of the D_2 and D_1 lines of Rb and the theoretical emission spectra from the vibrational levels of Rb*He shown in Fig. 2.

Figure 8 shows emission spectra measured at $T < 2.1$ K in the case of the D_2 excitation. These were measured with the spectrometer-CCD system. The observed spectra have structure resulting from the vibrational levels of Rb*He, as described in Secs. IV B and IV E. Similar emission spectra were observed after the D_2 excitation of Rb atoms on He droplets [6]. The spectral profile shown in Fig. 8 is strongly dependent on T, especially at $T < T_c$ ($= 1.9$ K), where the He gas density in the cell drastically changes with T as shown in Fig. 5(b). To distinguish the He gas density dependence from the temperature dependence, we measured emission spectra using another cell for which $T_c = 1.7$ K. The observed spectra were nearly the same as the spectra shown in Fig. 8 at $T \lesssim 1.7$ K, but were approximately independent of T for 1.7 K $< T <$ 2.1 K. Thus, it is concluded that the temperature dependence at $T < T_c$ is caused by the change of the He gas density.

B. Assignment of the observed spectra

We start with the component at 11 820 cm^{-1} (FWHM $= 610$ cm^{-1}), which is seen over a wide temperature range [see Figs. 7(a) and 7(b)]. This component is assigned to the emission from the $A\,^2\Pi_{1/2}v = 0$ state of Rb*He. As already mentioned in Sec. II, there are two attractive electronic states $A\,^2\Pi_{3/2}$ and $A\,^2\Pi_{1/2}$ for Rb*He (and also for Rb*He$_2$). The reason why the component is assigned to the emission from

the $A\,^2\Pi_{1/2}$ state is that it was observed in both cases of the D_2 and D_1 excitations. This discussion is based on the fact that in the case of the D_1 excitation, the D_2 emission line was not observed at $T \lesssim 40$ K, implying that Rb*He($A\,^2\Pi_{3/2}$) was not produced by collisional excitation of fine-structure transition. The assignment is supported by a good agreement between the wave number at peak and FWHM of the observed component and those of the calculated spectrum from the $A\,^2\Pi_{1/2}v = 0$ state; 11 880 cm^{-1} and 453 cm^{-1}, respectively (see Fig. 2).

The spectra observed at $T < 2.1$ K shown in Fig. 8 are considered to be superpositions of several components from the vibrational levels of Rb*He (see Fig. 2). The He gas density dependence can be understood as a change in the population distribution over the vibrational levels, as described in detail in Sec. IV E. At a low value of the He gas density ($T \lesssim 1.7$ K), we observed an emission spectrum in the wave number region between the D_2 and the D_1 lines (mainly on the red wing of the D_2 line). This emission originates from the high vibrational levels ($v \geq 2$) of the $A\,^2\Pi_{3/2}$ state. As the He gas density increased, the spectrum at 11 820 cm^{-1} originating from the $A\,^2\Pi_{1/2}v = 0$ state became dominant.

Among the components from the vibrational levels of Rb*He, the component from the $A\,^2\Pi_{1/2}v = 0$ state was dominant also at $T \geq 2$ K. It is natural to think that emission from Rb*He$_n$ ($n \geq 2$) also has its origin mainly in the vibrational ground state at $T \geq 2$ K. Our assignment in the following is based on this approximation. Thus, we compare the peak position of the observed spectral component, shown in Figs. 7(a) and 7(b), with that of theoretical spectrum from the vibrational ground state of Rb*He$_n$ ($n \geq 2$), shown in Fig. 4.

The component at 10 810 cm^{-1} is assigned to Rb*He$_2$ by comparison of the experimental and theoretical peak positions. This component was observed also in both cases of the D_2 and D_1 excitations, and thus is assigned to the emission from the $A\,^2\Pi_{1/2}$ state, based on the same discussion as above.

Another component at about 10 000 cm^{-1}, which is identified only at around 25 K, is assigned to Rb*He$_3$. Difference between the observed and theoretical wave numbers at peak, however, is larger than in the cases of $n = 1, 2$.

The other clearly identified is a component at 7300 cm^{-1} and with FWHM of about 1400 cm^{-1}, which is seen at $T \lesssim 10$ K. This component agrees well with the spectrum observed in liquid He shown in Fig. 6. Therefore, the component is the emission from Rb*He$_{n_{max}}$.

The broad spectra with a peak in the wave number region from 7300 cm^{-1} to 10 000 cm^{-1}, which were observed at 10 K $< T <$ 25 K, are superpositions of several components. The observed peak shift with T is due to a change in the relative intensities of the components. Since FWHM of each component is estimated to be, at most, 1400 cm^{-1} (the value for Rb*He$_{n_{max}}$), at least two components are required to exist between the spectra of Rb*He$_3$ and Rb*He$_{n_{max}}$ to explain the smooth peak shift. The difference spectrum between at 26 K and 28 K indicates the existence of a component at
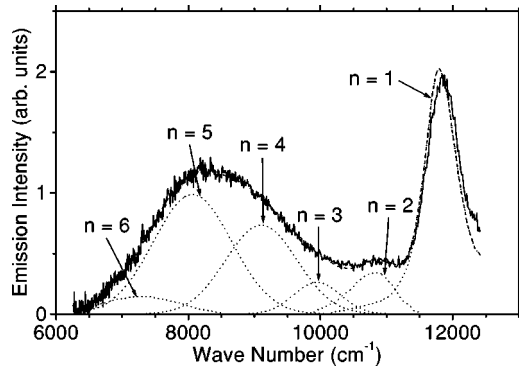
FIG. 9. Example of the fitting result. The solid line shows the spectrum observed at 19 K in the case of the D_2 excitation. The atomic D lines, which were not considered in the fitting, have been removed from the spectrum. The best-fitted curve (dashed line) consists of the six components for Rb*He$_n$ ($n=1-6$) (dotted lines). The three components for $n=3-5$ are Gaussian functions determined by the fitting, and the other three for $n=1,2,6$ are experimentally determined profiles which were used in the fitting.

about 9000 cm^{-1}, in the red tail of the Rb*He$_3$ component. The same component can be seen in the difference spectrum between at 17 K and 19 K. Similarly, the existence of a component at about 8100 cm^{-1} is indicated by comparing the spectrum at 14 K (21 K) with that at 10 K (22 K). We do not consider that there exists another component besides the two components, for the following reasons:

(1) If we assume that the above two components exist between the spectra of Rb*He$_3$ and Rb*He$_{n_{max}}$, the wave number interval between neighboring spectral peaks becomes nearly equal. This agrees with a theoretical result that the interval of the peak positions is approximately equal for different n as far as $n \lesssim n_{max}(=6)$.

(2) The theoretical suggestion that $n_{max}=6$ indicates the existence of two components.

(3) It is probable that the wave number at peak of the theoretical spectrum of Rb*He$_{n_{max}}$ deviates toward red from the observed, as seen for the component of Rb*He$_3$. To minimize this deviation, the condition $n_{max}=6$ gives the best result.

Thus, we finally conclude that the components at 9000 cm^{-1}, 8100 cm^{-1}, and 7300 cm^{-1} are from Rb*He$_4$, Rb*He$_5$, and Rb*He$_6(n_{max}=6)$, respectively.

In order to know the peak position and width of each component of spectra, we fitted to the observed spectra superpositions of six spectral components: three Gaussian curves for $n=3-5$ and three experimentally determined profiles for $n=1,2,6$. For $n=1$, the profile observed at 50 K was used. The profile for $n=2$ was obtained by subtracting the spectrum at 50 K from that at 5 K in the case of the D_2 excitation. For $n=6$, the profile at 5 K for the D_2 excitation was used. The fitting parameters were the wave numbers at center and FWHMs of the three Gaussian functions, and the relative intensities of the six components ($n=1-6$) of each spectrum. Figure 9 shows an example of the best-fitted curve, together with the resulting three Gaussian curves for $n=3-5$ and the profiles for $n=1,2,6$ used in the fitting. The
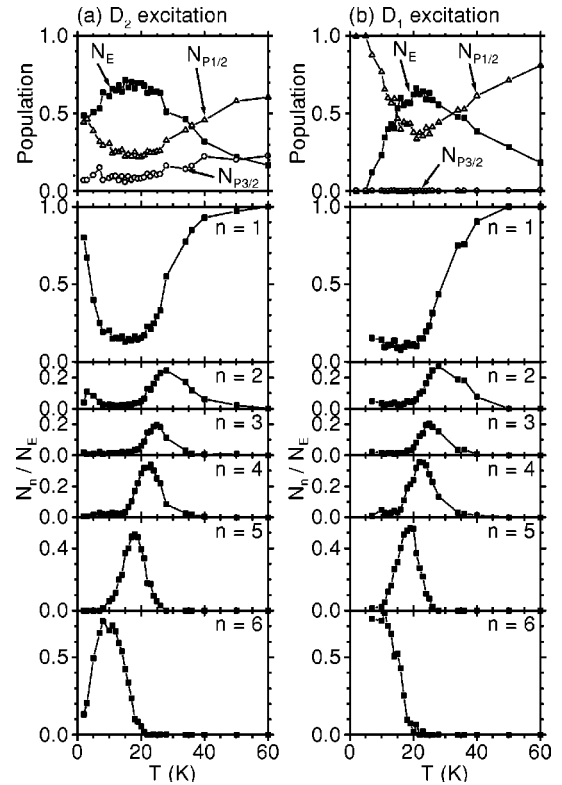
FIG. 10. Populations as functions of T in the cases of the D_2 excitation (a) and D_1 excitation (b). The N_n ($n=1-6$) is the relative population of Rb*He$_n$, and $N_{P3/2}$ and $N_{P1/2}$ are those of Rb($5\,^2P_{3/2}$) and Rb($5\,^2P_{1/2}$), respectively. The N_n has been normalized by the total population $N_E(=\Sigma_{n=1}^6 N_n)$ of Rb*He$_n$.

obtained wave numbers at center and FWHMs are 9949 cm^{-1} and 836 cm^{-1} for $n=3$; 9105 cm^{-1} and 1278 cm^{-1} for $n=4$; and 8065 cm^{-1} and 1398 cm^{-1} for $n=5$.

The discrepancy between the experimental and theoretical wave numbers at peak becomes larger as n increases from 1 to 6. We consider that this is due to the accumulation of error in the theoretical calculation with the increase of n.

C. Temperature dependence

The T dependence of the observed spectra shown in Figs. 7(a) and 7(b) is understood as the T dependence of relative populations of Rb*He$_n$ ($n=1-6$). We will write the relative populations of Rb*He$_n$ as N_n ($n=1-6$), and those of Rb($5\,^2P_{3/2}$) and Rb($5\,^2P_{1/2}$) as $N_{P3/2}$ and $N_{P1/2}$. We estimated these populations from the relative intensities of the six spectral components determined by the fitting and of the atomic D lines, taking into account the ν^3 dependence of radiative decay rate. With respect to the radiative decay rate A_n of Rb*He$_n$ ($n=1-6$), the electric dipole transition moment of Rb-He$_n$ was assumed to be equal to that of the Rb $5\,^2P$-$5\,^2S$ transition.

Figures 10(a) and 10(b) show the obtained relative populations as functions of T, in the cases of the D_2 and D_1 excitations, respectively. Note that each population N_n ($n=1-6$) is normalized by the total population of exciplexes,

$N_E = \Sigma_{n=1}^{6} N_n$. In the case of the D_2 excitation, N_E has a maximum of about 0.7 around 15 K. On the other hand, in the case of the D_1 excitation, N_E increases from zero as T rises above 5 K, and has a maximum of about 0.65 around 21 K. As T increases above 21 K, it falls in the same way as in the case of the D_2 excitation. In the temperature range $T > 5$ K where the emission from Rb*He$_n$ could be observed in both cases of the D_2 and D_1 excitations, temperature dependence of the ratios N_n/N_E ($n = 1$–6) is about the same for both cases. This is because, even in the case of the D_2 excitation, most excimers Rb*He produced in the $A\,^2\Pi_{3/2}$ state relax to the $A\,^2\Pi_{1/2}$ before emitting fluorescence or producing Rb*He$_2$ (at $T \gtrsim 2$ K), and hence there is no difference in the successive formation process from the case of the D_1 excitation.

At $T \lesssim 10$ K, the populations of $n = 1,2,6$ are dominant, and the populations of $n = 3$–5 are negligibly small. The ratio N_6/N_E greatly increases with increasing T above 2 K, until it becomes about 0.7 at around 10 K. This high ratio indicates the accumulation of the population of the terminal exciplex Rb*He$_{n_{max}}$ ($n_{max} = 6$). As T increases above 10 K, the populations of $n = 5,4$, and 3 begin to increase in this order, and the population shifts gradually from $n = 6$ to $n = 1$. This corresponds to the observed peak shift of the broad spectrum. When T rises above 40 K, $N_1 (\approx N_E)$ decreases rapidly.

We estimate here rate coefficient R_n for the formation process Rb*He$_{n-1} \rightarrow$ Rb*He$_n$, by substituting the obtained values of the relative populations into rate equations in steady state. We consider a temperature range of $T \lesssim 15$ K and assume that the dissociation processes Rb*He$_n$ $\rightarrow$ Rb*He$_{n-1}$ ($n = 1$–3) are negligible in this temperature range. Then, the rate coefficients for $n = 1$–3 can be expressed as

$$R_n = \frac{\sum_{k=n}^{6} N_k A_k}{N_{n-1}}, \tag{1}$$

where N_0 (for $n = 1$) corresponds to the population of the Rb-5 ^2P states. The N_0 for the D_2 excitation case is given by $N_{P3/2}$, within the temperature range $T \lesssim 5$ K where the formation of Rb*He$_n$ from Rb(5 $^2P_{1/2}$) is negligible. Thus, obtained values are $R_1 \approx 8 \times 10^7$ s^{-1}, $R_2 \approx 1 \times 10^7$ s^{-1}, and $R_3 \approx 4 \times 10^7$ s^{-1}, at 5 K. We see that these values are comparable to radiative decay rates, as expected. (The radiative rate for the atomic D_2 transition is 3.7×10^7 s^{-1} [21].) It is noted also that as T increases from 2 K to about 13 K, R_3 greatly increases from about 3×10^7 s^{-1} to 3×10^8 s^{-1}.

D. Dynamics of the exciplex formation

First, let us consider the decrease of N_E for the D_1 excitation with decreasing T below 21 K. This decrease is explained by the existence of the potential barrier (26.5 cm^{-1}) in the $A\,^2\Pi_{1/2}$ state of Rb*He. Due to the existence of the barrier, the formation of Rb*He decreases with the decrease of T. Larger exciplexes Rb*He$_n$ ($n = 2$–6) are produced

through Rb*He, so that the decrease in the formation of Rb*He leads to the decrease of N_E.

Next, we will discuss the experimental fact that the populations of $n = 3$–5 are negligibly small at $T \lesssim 10$ K. This indicates that the formation rates R_4, R_5, and R_6 are much larger than R_3, R_2, and R_1. To understand this difference in the formation rate, let us discuss in the following the formation process Rb*He$_{n-1}$ + He $\rightarrow$ Rb*He$_n$ ($n = 2$–6) in terms of the potential energy of the system Rb*He$_{n-1}$-He. The interaction between Rb and He is expressed mainly by the van der Waals attraction and the repulsion due to the Pauli exclusion principle. A He atom can approach the Rb core through the region where the Rb valence electron density is small. This simple description gives us a qualitative understanding of the formation process, as described below.

Let us begin with the process Rb*He + He $\rightarrow$ Rb*He$_2$. For both states $A\,^2\Pi_{1/2}$ and $A\,^2\Pi_{3/2}$ of Rb*He, the wave function of the Rb* valence electron is well expressed by the spherical harmonics $Y_1^{\pm 1}$, where the quantization axis is taken to the molecular axis of Rb*He. Its density distribution has an "applelike" shape. Therefore, it is possible for the second He atom to approach the Rb core without going over a potential barrier, as long as it comes to the other side of the first He atom.

When the third He atom approaches the Rb core, the situation is different from the case of the second He, because two potential minima are already occupied by the two He atoms. Therefore, we consider that the third He atom has to go over a potential barrier in order to stick to the Rb core. To obtain a quantitative estimation of the barrier, we calculated potential-energy surface for the system Rb*He$_2$-He. It should be mentioned that the barrier becomes higher as the fine-structure splitting Δ becomes larger. As mentioned in the introduction, we are thus interested in comparing the result with the potential surface for Cs*He$_2$-He, which is presented in Sec. IV F.

In the calculation, we fixed the Rb* at $(y,z) = (0,0)$ and the two He atoms of Rb*He$_2$ at equilibrium positions $(0, \pm r_0)$ ($r_0 = 3.24$ Å). The third He atom was located on the y-z plane, and we will express its position as $(r \sin\theta, r \cos\theta)$. As in Sec. II, *ab initio* potential energies of the excited states were calculated at the RHF level [11], and the spin-orbit interaction was taken into account.

Figure 11(a) shows a contour map of the obtained potential-energy surface of the lowest excited state in the region of $0° \leq \theta \leq 90°$. As expected, we see that the third He atom has to go over a potential barrier before entering a potential well in the region of $r \approx r_0$ and $\theta \gtrsim 45°$. The saddle point is located at $r = 4.9$ Å and $\theta = 38°$, and the energy of the point (maximum energy along the minimum energy path for the formation) is 20.5 cm^{-1} above the dissociation limit Rb*He$_2$ ($A\,^2\Pi_{1/2}$) + He. As already mentioned, the formation rate R_3 greatly increases as T increases from 2 K to about 13 K. The existence of the barrier may be the reason for this. The potential well has a minimum at $r = 3.24$ Å and $\theta = 65°$ with a depth of 114.4 cm^{-1} below the saddle point. There exist several bound states in this potential well.
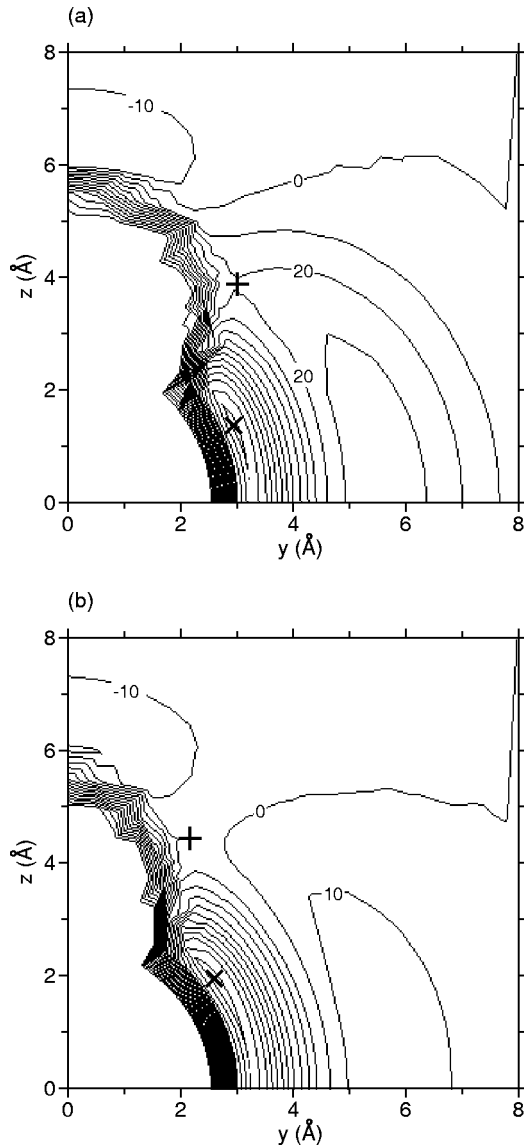
FIG. 11. Potential-energy surfaces calculated for the system Rb*He$_2$-He. The Rb* was fixed at $(y,z)=(0,0)$ for both (a) and (b). The two He atoms of Rb*He$_2$ were fixed at $(0,\pm3.24)$ in the case of (a), and at $(0,-3.24)$ and $(-3.24\sin11°, 3.24\cos11°)$ in the case of (b) (all in units of Å). The energy is in units of cm^{-1} and the zero of energy is at each dissociation limit Rb*He$_2$+He. The contour interval is 10 cm^{-1}. The marks "+" and "×" show the positions of saddle point and potential minimum, respectively.

Up to now we have fixed the two He atoms of Rb*He$_2$ at their equilibrium positions. During the formation process of Rb*He$_3$, however, they can move in the depressions of the applelike density distribution of the Rb valence electron. To estimate this effect on the potential barrier, we considered the vibration in Rb*He$_2$. The most important vibrational mode for lowering the potential barrier is the bending vibration, and the one in the y-z plane under the present configuration of the atoms. We took into account only its zero-point vibration, because the energy needed to excite the vibration, $\Delta\epsilon_b=34.5$ cm^{-1}, is large compared with the thermal energy at $T\lesssim30$ K. Setting the bending angle to the value corre-

sponding to the classical turning point ($\angle$He-Rb-He $=169°$), we calculated the potential surface for the third He atom on the y-z plane. The result is shown in Fig. 11(b). The energy of the saddle point is lowered to 3.4 cm^{-1} below the dissociation limit Rb*He$_2$ (bended) + He. The cross section for the formation of Rb*He$_3$ might, however, be small even in this extreme case, due to the narrow channel in the vicinity of the saddle point.

Now let us consider the reason why R_4, R_5, and R_6 are larger than R_3, comparing the formation processes of Rb*He$_3$ and Rb*He$_n$ ($n=4-6$). A significant difference between $n=3$ and $n=4-6$ is the density distribution of the Rb valence electron of the preceding exciplexes Rb*He$_2$ and Rb*He$_n$ ($n=3-5$). As already mentioned in Sec. II, the density distribution for Rb*He$_n$ ($n=3-5$) is well expressed by that of the p_x orbital, under the condition that the n He atoms are located on the y-z plane and on a circle with the center at the position of Rb. The "dumbbell-like" density distribution presents around its neck a potential well for He atoms. According to the pair potential of Rb*-He calculated in Sec. II, the depth of the potential minimum for the p_x orbital is 176.8 cm^{-1}. Even at low temperatures, He atoms are energetically allowed to approach this potential well through the nodal y-z plane of the p_x orbital. This is in contrast to the formation of Rb*He$_3$ described above. The rearrangement of He atoms would proceed more easily than in the case of the formation of Rb*He$_3$, because He atoms in the potential well can move along the circle more freely than those in the depressions of the applelike density distribution for Rb*He$_2$. Furthermore, the number of vibrational modes of the preceding exciplex Rb*He$_{n-1}$ increases with increasing n. This is favorable for the efficient release of the translation and binding energies between Rb*He$_{n-1}$ and He, during the formation process of Rb*He$_n$.

Finally, let us consider the experimental fact that the population shifts from $n=6$ to $n=1$, as T increases from 10 K to about 40 K. In this temperature range, the thermal energy is of the same order of magnitude as the energy difference ΔE_n (see Sec. II), which gives the energy required to dissociate a He atom of Rb*He$_n$ from the Rb core. As a result, the rate for collision-induced dissociation process Rb*He$_n$+He→Rb*He$_{n-1}$+He+He rises as T increases. In addition, the rate for the formation process Rb*He$_{n-1}$+He →Rb*He$_n$ falls with the increase of T, because the kinetic energy of translation between Rb*He$_{n-1}$ and He can be used to dissociate any one of the $n-1$ He atoms from the Rb core. Such a temperature dependence of the dissociation and formation rates explains the fact that the population shifts from n to $n-1$ with increasing T. This discussion applies also to the case of $n=1$: the calculated binding energy of Rb*He (see Table I), which corresponds to the energy ΔE_1, explains the decrease of N_1 with increasing T above 40 K. We believe that Rb*He$_7$ should hardly be populated, even when T increases from about 10 K and the thermal energy becomes comparable to $-\Delta E_7$ (see Fig. 3). Under this situation, the thermal energy becomes also comparable to ΔE_6, which results in the decrease of N_6. As a result, the production of

(a)

(b)
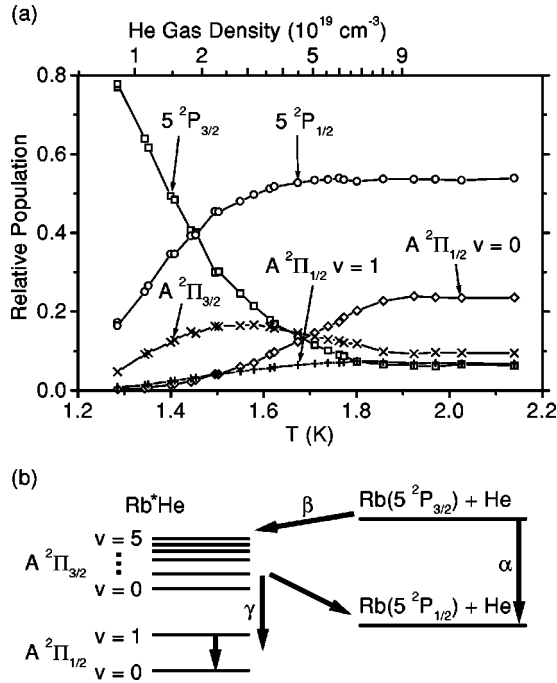
FIG. 12. (a) Relative populations of the vibrational levels of Rb*He and the $5\ ^2P$ states of Rb, in the case of the D_2 excitation. As for the $A\ ^2\Pi_{3/2}$ state of Rb*He, the total population of the four vibrational levels ($0 \leq v \leq 3$) is shown. (b) Relaxation processes in the excited states after the D_2 excitation of Rb. With respect to the three processes labeled by α, β, and γ, the rate coefficients were estimated (see text).

Rb*He$_7$ is also suppressed, since Rb*He$_7$ is created via Rb*He$_6$.

E. He gas density dependence

As already mentioned, in the case of the D_2 excitation, the temperature dependence of the spectra of Rb*He at $T < T_c$ ($= 1.9$ K) (see Fig. 8) is caused mainly by a change of the He gas density [see Fig. 5(b)]. The He gas density dependence of the spectra is due to a change in the population distribution over the vibrational levels of Rb*He. In order to obtain the populations, we fitted to each spectrum a superposition of the atomic D_2 and D_1 lines and the theoretical emission spectra from the vibrational states of Rb*He shown in Fig. 2. The fitting parameters were the relative populations of the $5\ ^2P_{3/2}$ and $5\ ^2P_{1/2}$ states of Rb and those of the vibrational states of Rb*He. The states $A\ ^2\Pi_{3/2} v = 4, 5$ of Rb*He were not taken into consideration: the wave number difference between the main peak of each theoretical spectrum and the center of the D_2 line was smaller than the spectral resolution of the detection system (≈ 20 cm^{-1}), and hence it was impossible to distinguish each spectrum from the D_2 line. The best-fitted curves are shown by dotted lines in Fig. 8, where we see that they are in good agreement with the observed spectra.

Figure 12(a) shows the obtained relative populations. As for the $A\ ^2\Pi_{3/2}$ state of Rb*He, the intensity of the spectral component from each vibrational level is weak, so that the relative population of each level is small (<0.07) and has

ambiguity. Therefore, only the total population of the $A\ ^2\Pi_{3/2}$ state is shown in Fig. 12(a). We see that, as the He gas density increases, (1) the population of Rb($5\ ^2P_{1/2}$) increases relatively to that of Rb($5\ ^2P_{3/2}$), (2) the total population of Rb*He increases relatively to that of the Rb-$5\ ^2P$ states, (3) the total population of Rb*He($A\ ^2\Pi_{1/2}$) increases relatively to that of Rb*He ($A\ ^2\Pi_{3/2}$), and (4) the population of the $A\ ^2\Pi_{1/2} v = 0$ state increases relatively to that of the $A\ ^2\Pi_{1/2} v = 1$. All of these are explained by the increase in the rates of collision-induced relaxation processes, which are shown by arrows in Fig. 12(b).

The fact that population is distributed over various states indicates that the relaxation rates are comparable to the radiative decay rate. We estimated the rate coefficients for the following three processes: α, for the fine-structure relaxation of Rb ($5\ ^2P_{3/2} \rightarrow 5\ ^2P_{1/2}$); β, for the formation of Rb*He [Rb($5\ ^2P_{3/2}$) + He $\rightarrow$ Rb*He($A\ ^2\Pi_{3/2}$)]; and γ, for the fine-structure relaxation of Rb*He ($A\ ^2\Pi_{3/2} \rightarrow A\ ^2\Pi_{1/2}$) [see Fig. 12(b)]. We considered the total populations of the states $A\ ^2\Pi_{3/2}$ and $A\ ^2\Pi_{1/2}$, respectively, neglecting vibrational structures. We substituted the values of the relative populations into rate equations in steady state obtained under the following assumptions.

(1) Rb*He ($A\ ^2\Pi_{1/2}$) is not produced directly from Rb($5\ ^2P_{3/2}$) + He, but produced through Rb*He ($A\ ^2\Pi_{3/2}$). This assumption is derived from the experimental fact that the total population of Rb*He ($A\ ^2\Pi_{1/2}$) is negligibly small, in spite of the large population of Rb($5\ ^2P_{3/2}$) at $T \lesssim 1.4$ K.

(2) Formation of Rb*He$_n$ ($n = 2-6$) from Rb*He is negligible. This is based on the fact that with respect to the spectrum at 2 K in Fig. 7(a), the integrated intensity of emission from Rb*He$_n$ ($n = 2-6$) is less than 4% of the total emission intensity.

(3) Any collisional excitation process is negligible in the temperature range $T < 2.1$ K.

We took into account also the experimental fact that Rb($5\ ^2P_{1/2}$) did not produce Rb*He at $T < 5$ K. Finally we obtained $\alpha \lesssim 6.9A$, $4.4A \lesssim \beta \lesssim 11A$, and $\gamma \approx 1.9A$ at 1.80 K, where A ($= 3.7 \times 10^7$ s^{-1}) is the radiative decay rate for the Rb D_2 transition.

The fine-structure changing process in cold and dense He has not been well investigated so far. Gallagher investigated the cross sections for the fine-structure changing of an alkali-metal atom ($^2P_{3/2} \rightarrow ^2P_{1/2}$) due to the binary collisions with a rare-gas atom at the temperature higher than a room temperature [26]. The extrapolation of his results to a low temperature suggests that α should be several orders of magnitude smaller than A when only the binary collisions are considered. Namely, the population ratio of Rb($5\ ^2P_{1/2}$) to Rb($5\ ^2P_{3/2}$) obtained in our experiment is much larger than that expected from above extrapolation. This discrepancy may suggest that there exists indirect fine-structure changing process through formation and dissociation of Rb*He, occurring only at a low temperature in high density He. The rate coefficient γ may also be increased by the similar process through the formation and dissociation of Rb*He$_2$.

F. Differences between Rb and Cs

Let us compare the results of the present work and our previous experiment with Cs, which was recently reported
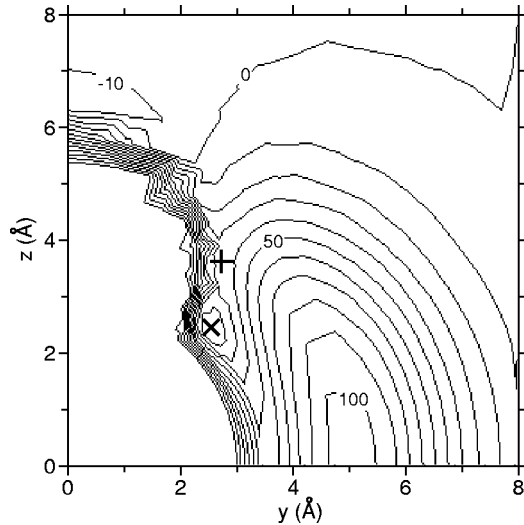
FIG. 13. Potential-energy surface calculated for the system Cs*He$_2$-He. The Cs* atom was fixed at $(y,z)=(0,0)$ and the two He atoms of Cs*He$_2$ were fixed at $(0,\pm 3.5)$, in units of Å. The energy is in units of cm^{-1} and the zero of energy is at the dissociation limit Cs*He$_2$ $(A\,^2\Pi_{1/2})+$He. The contour interval is 10 cm^{-1}. The marks "+" and "×" show the positions of saddle point and potential minimum, respectively.

[9]. The Cs cell used in the previous experiment contained about the same amount of He as the present work. The important point to understand the difference between the results for Rb and Cs is that the fine-structure splitting of the Cs-6$\,^2P$ states ($\Delta=554.0$ cm^{-1}) is larger than that of the Rb-5$\,^2P$ states ($\Delta=237.6$ cm^{-1}).

First, it has been found that n_{max} is 6 for Rb and 2 for Cs. To compare the formation processes of Rb*He$_3$ and Cs*He$_3$, numerical calculation of the potential-energy surface was carried out for the system Cs*He$_2$-He. As in the calculation for Rb*He$_2$-He (see Sec. IV D), we fixed the Cs* at $(y,z)=(0,0)$ and the two He atoms of Cs*He$_2$ at equilibrium positions $(0,\pm r_0)$ ($r_0=3.5$ Å). We calculated the potential energy of the system by summing over all pair interactions, and took into account the spin-orbit interaction of the Cs-6$\,^2P$ states. We used potential energies calculated by Pascale [10] for the Cs*-He interactions, and the analytical Hartree-Fock-dispersion individual-damping form of the pair potential of Aziz and Slaman [27] for the He-He interactions. Figure 13 shows the potential-energy surface obtained for the lowest excited state. Due to the larger splitting Δ, the potential barrier is higher than that for Rb*He$_2$-He. The saddle point is located at $r=4.5$ Å and $\theta=37°$, and the energy of the point is 33.1 cm^{-1} above the dissociation limit Cs*He$_2$ $(A\,^2\Pi_{1/2})+$He. The larger value of the splitting results in also the narrower and shallower potential well which has a minimum at $r=3.5$ Å and $\theta=46°$ with a depth of 22.4 cm^{-1} below the saddle point. It should be noted that there exists no vibrational state in this well. As in Sec. IV D, we considered the bending vibration in Cs*He$_2$ ($\Delta\epsilon_b=26.2$ cm^{-1}), setting the bending angle to the value of the classical turning point for the zero-point vibration ($\angle$He-Cs-He$=167°$). The energy of the saddle point is low-

ered to 7.6 cm^{-1} above the dissociation limit Cs*He$_2$ (bended)$+$He. Nevertheless, there still does not exist a vibrational state in the well. We consider that the absence of the vibrational state prevents the formation of Cs*He$_3$. As already mentioned, the potential well has several bound states in the case of Rb. This difference explains well why $n_{max}=2$ for Cs, while $n_{max}>2$ for Rb.

Second, in the case of the D_1 excitation, the integrated intensity of emission from Rb*He$_n$ ($n=1$–6) accounted for about 50% of the total emission intensity at $T\approx 25$ K, whereas the emission from Cs*He$_n$ ($n=1,2$) was only about 1% at maximum. This is because the potential barrier in the $A\,^2\Pi_{1/2}$ state of Cs*He (75.2 cm^{-1}) [9] is higher than that of Rb*He (26.5 cm^{-1}), due to the larger splitting Δ.

A similar effect of the potential barrier in the $A\,^2\Pi_{1/2}$ state was indicated by experiments with He droplets [28]. With respect to the D_1 excitation of alkali atoms on He droplets, the photoinduced desorption of K*He took place more slowly than that of Na*He [28], and emission from Rb*He was not observed [6]. These were explained by the existence of a similar potential barrier in the $A\,^2\Pi_{1/2}$ state.

Finally, we estimated the three relaxation rate coefficients α, β, and γ in the case of Cs, using the same method as described in Sec. IV E. The $A\,^2\Pi_{1/2}v=0$ state of Cs*He is a quasibound state, so we took into consideration also the predissociation process Cs*He $(A\,^2\Pi_{1/2})\rightarrow$Cs$(6\,^2P_{1/2})+$He [9], which was not considered in the case of Rb. From the emission spectrum observed at 1.81 K for the D_2 excitation of Cs, we obtained $\alpha\lesssim 2.0A'$, $16A'\lesssim\beta\lesssim 18A'$, and $0.58A'\lesssim\gamma\lesssim 0.76A'$, where $A'(=3.7\times 10^7$ s$^{-1})$ is the radiative decay rate for the Cs D_2 transition $(6\,^2P_{3/2}\rightarrow 6\,^2S_{1/2})$ [21]. The rate coefficient γ for the fine-structure relaxation of Cs*He is less than half of that of Rb*He. This is qualitatively consistent with a prediction derived from the adiabaticity parameter [29], which tells us that the probability of nonadiabatic transition decreases with an increase in the transition energy (roughly expressed by Δ in the present case).

V. CONCLUSION

We have reported on the emission spectra of Rb*He$_n$ observed when Rb atoms were excited to the $5\,^2P$ states in a cryogenic ^{4}He gas. By observing the spectra at various temperatures ($T\lesssim 100$ K) and with the help of *ab initio* potential calculation, we have assigned the spectra of all of Rb*He$_n$ ($n=1$–6). We have found that the emission spectrum of the exciplex in liquid He agrees with that of Rb*He$_6$, and this is consistent with our theoretical result that the vibrational ground state of Rb*He$_6$ has the lowest-energy level among all n.

From the spectral profiles, the relative population for each n and the exciplex formation rate coefficient R_n for Rb*He$_{n-1}+$He$\rightarrow$Rb*He$_n$ have been estimated. Especially, we have paid attention to the process of Rb*He$_2+$He $\rightarrow$Rb*He$_3$, since R_3 depends strongly on the temperature between 2 K and 13 K. We have calculated the potential-energy surface for the system Rb*He$_2$-He, and have found that the strong temperature dependence of R_3 is considered

to be due to a potential barrier in this formation process, which originates from the spin-orbit coupling. By performing similar calculation for the system Cs*He$_2$-He which has a larger spin-orbit coupling strength, we have found that there is no bound state under the assumption that the bending angle of Cs*He$_2$ is within the range of the zero-point bending vibration. This can explain well the experimental fact that Cs*He$_3$ is not produced [9].

At $T < T_c (= 1.9$ K), where the He gas density in the cell varies, we observed also vibrational structure in the emission spectra of Rb*He, which was strongly dependent on the He gas density. We have obtained the population for the vibrational states of the $A\ ^2\Pi_{1/2}$ and $A\ ^2\Pi_{3/2}$ states, and estimated the rate coefficient for the fine-structure changing process of Rb*He. This rate coefficient has also been estimated for Cs*He.

Through a comparison with our previous work with Cs [9], it has become clear that the spin-orbit interaction plays an important role in alkali-atom-He$_n$ exciplex formation. For example, potential barriers originating from the spin-orbit coupling make difference in n_{max} between Rb and Cs, and prevent exciplex formation after the D_1 excitation at $T < 10$ K for Rb and at any temperature for Cs. As an alkali-

metal atom becomes smaller, the fine-structure splitting Δ of the first P states becomes smaller, and thus its contribution to the potential energy becomes smaller. Therefore, experiments with K ($\Delta = 57.7$ cm^{-1}) and Na ($\Delta = 17.2$ cm^{-1}), now underway in our laboratory, will help to understand further the effects of the spin-orbit interaction.

[1] H. Bauer, M. Beau, J. Fischer, H.J. Reyher, J. Rosenkranz, and K. Venter, Physica B **165-166**, 137 (1990).

[2] Y. Takahashi, K. Sano, T. Kinoshita, and T. Yabuzaki, Phys. Rev. Lett. **71**, 1035 (1993).

[3] S. Kanorsky, A. Weis, M. Arndt, R. Dziewior, and T.W. Hänsch, Z. Phys. B: Condens. Matter **98**, 371 (1995).

[4] J. Dupont-Roc, Z. Phys. B: Condens. Matter **98**, 383 (1995).

[5] T. Kinoshita, K. Fukuda, T. Matsuura, and T. Yabuzaki, Phys. Rev. A **53**, 4054 (1996).

[6] F.R. Brühl, R.A. Trasca, and W.E. Ernst, J. Chem. Phys. **115**, 10 220 (2001).

[7] Z.J. Jakubek, Q. Hui, and M. Takami, Phys. Rev. Lett. **79**, 629 (1997).

[8] J.L. Persson, Q. Hui, Z.J. Jakubek, M. Nakamura, and M. Takami, Phys. Rev. Lett. **76**, 1501 (1996).

[9] K. Enomoto, K. Hirano, M. Kumakura, Y. Takahashi, and T. Yabuzaki, Phys. Rev. A **66**, 042505 (2002).

[10] J. Pascale, Phys. Rev. A **28**, 632 (1983).

[11] H.-J. Werner, P.J. Knowles, R.D. Amos, A. Bernhardsson, A. Berning, P. Celani, D.L. Cooper, M.J.O. Deegan, A.J. Dobbyn, F. Eckert, C. Hampel, G. Hetzer, T. Korona, R. Lindh, A.W. Lloyd, S.J. McNicholas, F.R. Manby, W. Meyer, M.E. Mura, A. Nicklass, P. Palmieri, R. Pitzer, G. Rauhut, M. Schütz, H. Stoll, A.J. Stone, R. Tarroni, and T. Thorsteinsson, computer code MOLPRO Ver. 2000. 1 (University of Birmingham, Birmingham, 2000).

[12] J.S. Binkley, J.A. Pople, and W.J. Hehre, J. Am. Chem. Soc. **102**, 939 (1980); W.J. Pietro, M.M. Francl, W.J. Hehre, D.J. DeFrees, J.A. Pople, and J.S. Binkley, *ibid.* **104**, 5039 (1982); K.D. Dobbs and W.J. Hehre, J. Comput. Chem. **7**, 359 (1986).

[13] W.J. Hehre, R. Ditchfield, and J.A. Pople, J. Chem. Phys. **56**, 2257 (1972); P.C. Hariharan and J.A. Pople, Theor. Chim. Acta **28**, 213 (1973).

[14] H.-J. Werner and P.J. Knowles, J. Chem. Phys. **82**, 5053 (1985); P.J. Knowles and H.-J. Werner, Chem. Phys. Lett. **115**, 259 (1985).

[15] H.-J. Werner and P.J. Knowles, J. Chem. Phys. **89**, 5803 (1988); P.J. Knowles and H.-J. Werner, Chem. Phys. Lett. **145**, 514 (1988).

[16] R.H.G. Reid, J. Phys. B **6**, 2018 (1973).

[17] R.E. Smalley, D.A. Auerbach, P.S.M. Fitch, D.H. Levy, and L. Wharton, J. Chem. Phys. **66**, 3778 (1977).

[18] D.L. Cooper, J. Chem. Phys. **75**, 4157 (1981).

[19] R. Brühl, J. Kapetanakis, and D. Zimmermann, J. Chem. Phys. **94**, 5865 (1991).

[20] P. Bauman, D. Zimmermann, and R. Brühl, J. Mol. Spectrosc. **155**, 277 (1992).

[21] A.A. Radzig and B.M. Smirnov, *Reference Data on Atoms, Molecules, and Ions* (Springer-Verlag, Berlin, 1985).

[22] R.J. Le Roy and G.T. Kraemer, University of Waterloo Chemical Physics Research Report No. CP-650R, 2001 (unpublished).

[23] G. Rauhut, A. El Azhary, F. Eckert, U. Schumann, and H.-J. Werner, Spectrochim. Acta **55**, 651 (1999).

[24] A. Hatakeyama, K. Enomoto, N. Sugimoto, and T. Yabuzaki, Phys. Rev. A **65**, 022904 (2002).

[25] T. Kinoshita, K. Fukuda, Y. Takahashi, and T. Yabuzaki, Phys. Rev. A **52**, 2707 (1995).

[26] A. Gallagher, Phys. Rev. **172**, 88 (1968).

[27] R.A. Aziz and M.J. Slaman, J. Chem. Phys. **94**, 8047 (1991).

[28] J. Reho, J. Higgins, K.K. Lehmann, and G. Scoles, J. Chem. Phys. **113**, 9694 (2000).

[29] H.S.W. Massey, Rep. Prog. Phys. **12**, 248 (1949).